Photocatalytic activity of ZnO nanomaterials with different morphologies

G. Gelashvili[a], D. Gelenidze[a], D. Jishiashvili[a,*], Z. Shiolashvili[b], N. Makhatadze[b], A. Jishiashvili[b], V. Gobronidze[b]
[a]Tbilisi State University, Andronikashvili Institute of Physics, 6 Mikheil Tamarashvili St., Tbilisi 0177, Georgia
[b]Georgian Technical University, Chavchanidze Institute of Cybernetics, 5 Z. Anjaparidze St., Tbilisi 0186, Georgia

The influence of ZnO nanomaterial morphologies on their photocatalytic activity was studied. The ZnO nanobelts and the network of hexagonal disks were grown by pyrolysis in ammonium chloride. ZnO tetrapods were produced by plasma-assisted technology. The nanobelts and tetrapod arms were growing along the c-axis. The sidewalls of nanobelts comprise $(2\bar{1}\bar{1}0)$ and $(01\bar{1}0)$ plane, while the needle-shape arms of tetrapods are known to consist of altering $\{01\bar{1}0\}$ and semi-polar $\{10\bar{1}1\}$ facets. The hexagonal ZnO disks have exposed mainly (+0001) facets with the highest surface energy. They showed the highest photocatalytic activity for the degradation of methylene blue, dissolved in water to a concentration of 100 mg/L.

1. Introduction

Bulk and nanosized zinc oxide is a well-studied, versatile and smart material with a wide range of industrial applications [1-4]. Because of its non-toxicity and high biocompatibility, the application range also includes medical and pharmaceutical usage [5-8]. The electrical, optical and chemical properties of nanosized ZnO strongly depend not only on its size and morphology but also on the surface area of exposed crystal facets [9-13]. To create nanomaterials with a high level of activity, careful control of a high-energy crystal plane exposure during the synthesis of ZnO is needed.

The growth of nanomaterials with different shapes proceeds as self-assembling processes governed not only by the thermodynamics and kinetics of synthetic reactions but also by electrostatic driving forces that arise between constituent species. As is well known, the last item is of particular importance for the growth of ZnO-based nanomaterials because the chemical bond between Zn and oxygen atoms has a high ionic and low covalent constituent. This results in the appearance of a natural dipole and in strong piezoelectric effects. The thermodynamically most stable wurtzite structure ZnO consists of alternating oxygen and Zn atomic layers stacked along the *c*-axis. This causes the formation of polar, oxygen terminated negatively charged (-0001), and positively charged Zn terminated (+0001) planes. The basal (+0001) plane has the highest surface energy of 2.25 J/m^2 as compared to the family of $\{01\bar{1}0\}$ (1.12 J/m^2) and $\{11\bar{2}0\}$ (1.06 J/m^2) prism planes [14]. Accordingly, the abundance of the non-polar $(11\bar{2}0)$ and $(10\bar{1}0)$ surfaces of wurtzite ZnO is due to their small surface energies. On the other hand, the fabrication of a catalyst with a large area of energetic (0001) facets is an important issue for the production of active photocatalysts, which may be used for the purification of wastewater [15,16].

The first purpose of this work was to study the morphology and structure of ZnO nanomaterials synthesized by pyrolytic and plasma deposition technologies. The second purpose

---

was to evaluate the activity of produced nanomaterials for photocatalytic decomposition of methylene blue dissolved in water.

2.Experimental

The pyrolytic technology was used for producing ZnO nanobelts and hexagonal plates. The details of this technology are described elsewhere [17]. It implied the application of a vertical quartz tube reactor, evacuated down to 2×10^{-5} Torr. The mixture of 99.999 purity Zn and ZnO powders, together with ammonium chloride (NH_4Cl) was placed on the bottom of the reactor. The total mass of the mixture was 2.1 g, while the mass of NH_4Cl was kept at 0.9g, and Zn:ZnO mass ratio was changed from 0.5 up to 2.0. The Si substrate was placed at 2-4 cm above the Zn source and its temperature was controlled by changing this distance. The source was heated to desired temperature (200-550°C) by an external resistive furnace. The growth process was controlled by varying the furnace temperature, Zn:ZnO ratio and source-substrate distance.

ZnO tetrapods were synthesized using the plasma arc burner. The details of this plasma-assisted technology are presented in [18].

The morphology and composition of synthesized nanomaterials were studied using the Scanning Electron Microscopy (SEM) (Tescan Vega 3 LMU) equipped with Oxford Systems Energy-Dispersive Spectrometer (EDS). The structure was analyzed by the Transmission electron microscope (TEM, Phillips CM-12) and X-ray diffractometer (XRD, Rigaku Smartlab-5).

For the evaluation of catalytic activity, the grown ZnO was scraped off from the substrate and mixed in the dark with the solution containing the known concentration of methylene blue. The concentration of the catalyst in the solution was kept at 100 mg/L. We irradiated the suspension for the pre-defined time and distance of 20cm, using the Xe lamp ДКсШ (100W) that served as the sunlight simulator because it emitted the light in the range close to the spectrum of the sun.

The small volumes of liquid were taken from the catalyst-dye suspension at certain time intervals and separated from the catalyst, then placed in the quartz cuvette and analyzed its optical absorbance at λ=662nm wavelength using UV-Vis spectrophotometer СФ-26.

The photodegradation (photodecolorization) rate was calculated as: $R(t)=[1-(A(t)/A(t_0)]\times100\%$, where $A(t_0)$ and $A(t)$ are the absorbance values at time t_0 and t respectively. The value of $R(t)$ is in fact equivalent to the mole percentage of degraded methylene blue. The details of the measurement are described in [19].

3. Results and discussion

SEM and TEM images of ZnO nanobelts, grown on the Si surface at a substrate temperature of 420°C and Zn:ZnO=1.6, are shown in Fig. 1. The widths of nanobelts vary in a wide range beginning from 30 nm up to 250 nm, while their thicknesses have a more narrow size distribution, and vary from 20 to 50 nm. The ball-shaped catalyst tips were observed for all nanobelts, indicating that they were grown by the Vapor-Liquid-Solid (VLS) mechanism. The tapering and kinks were also observed in nanobelts.
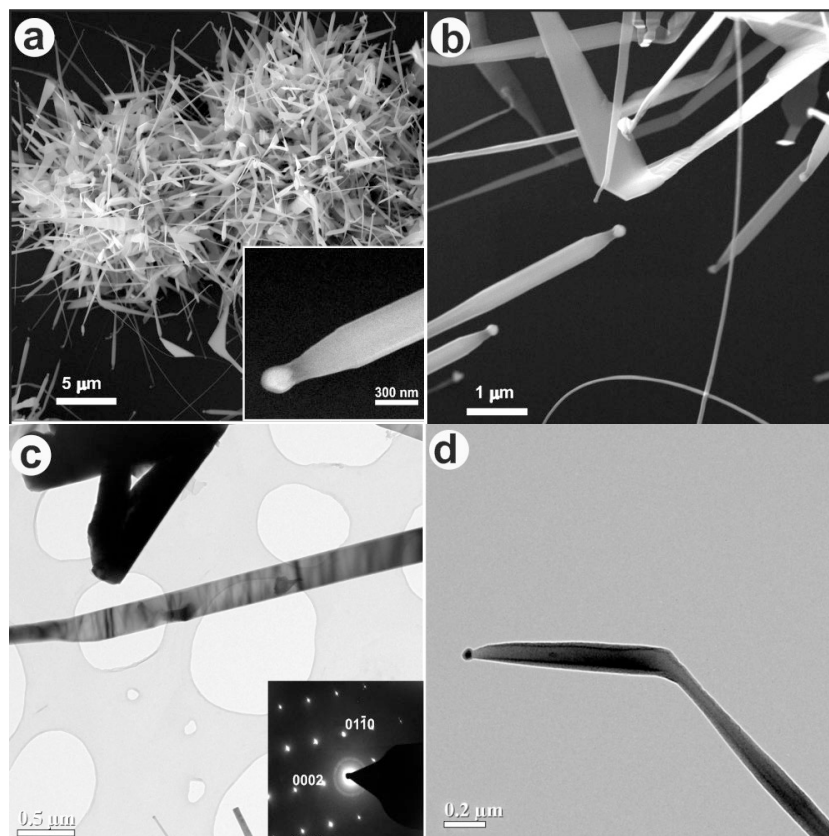
Fig. 1. SEM (a,b) and TEM (c,d) images of VLS grown ZnO nanobelts. The SAED pattern is shown in the inset of Fig. 1(c).

The composition of nanobelts was analyzed by EDS method (the data are not presented). As it was expected, the tip comprises a Zn-rich catalyst. The concentration of oxygen in the nanobelt body was 5 at.% higher (47 at.% Zn and 53 at.% oxygen) than in stoichiometric ZnO. The exposure to the atmosphere followed by the adsorption of oxygen when loading a sample into the microscope for EDS analysis can explain the observed increase in oxygen content.

The Selected Area Electron Diffraction (SAED) pattern of nanobelts is shown in the inset of Fig. 1c. It confirms the hexagonal wurtzite structure of nanobelts. They grow along the c-axes ([0001] direction), which is the most commonly observed and fastest growth direction for ZnO nanobelts. As for the sidewalls of the nanobelt, the wide front plane is indexed as the $(2\bar{1}\bar{1}0)$ one, while the sidewall comprises $(01\bar{1}0)$ plane.

The next nanomaterial that was used for the photocatalytic decomposition of water contaminants is shown in Fig. 2. It comprises hexagonal ZnO disks with an average thickness of 200 nm and a mean diameter of 1.5 micrometers. The substrate temperature was again 420°C, while the Zn:ZnO mass ratio in the source was reduced to 0.5. The SEM images of this nanomaterial are presented in Fig. 2a and its lower insets. The network of hexagonal plates is easily visible.
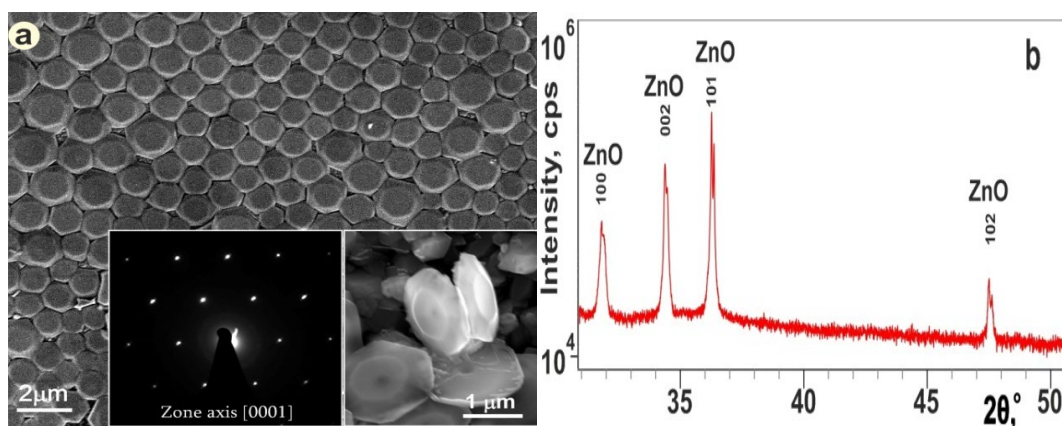
Fig. 2. (a) SEM image of hexagonal ZnO disks. The right and left insets show the magnified view of nanodisks and their SAED pattern; (b) the XRD pattern of ZnO hexagonal disks (b).

The lower inset of Fig. 2a shows the selected area electron diffraction pattern, taken along the *c*-axis ([0001] direction) which proves the formation of hexagonal ZnO. The XRD pattern is presented in Fig. 2b, which again confirms the growth of hexagonal, wurtzite structure ZnO plates with exposed (0001) plane and its good crystallinity. No phase other than wurtzite ZnO was detected. A slight increase of (0002) plane-related peak in Fig. 2b as compared to standard XRD data ((JCPDS 36–1451) indicates the prevalence of basal planes in the grown ZnO. As previously mentioned, the basal Zn-terminated and positively charged (0001) plane has the highest surface energy and growth rate. In the fast, kinetically driving growth processes the growing ZnO crystal tries to minimize the surfaces with high energy. This causes the gradual decrease of the 0001 plane, and tapering of a crystal until complete elimination of this surface. The described process significantly decreases the surface energy, and thus the ZnO crystal usually grows along the *c*-axis. On the other hand, the polarized (0001) plane is more sensitive to charged molecules and light interaction. Besides, according to theoretical results, this plane is characterized by a higher mobility and lower recombination rate making crystals with exposed (0001) facets more attractive for devices exploiting photostimulation and catalytic effects [20,21].

In spite of these advantages, the synthesis of ZnO crystals with large (0001) surfaces is a quite complicated task, as it needs the suppression of thermodynamically preferable growth along the *c*-axis, thus forcing the crystal to grow laterally. This task was successfully solved in solvothermal growth processes by applying the cap layers containing KCl, NH_3, Cl ions and some other species [22,23], which after preferentially adsorbing onto the (0001) plane, hindered its perpendicular growth. As a result, the growth proceeded mainly laterally, producing two-dimensional, planar, hexagonal, or rectangular structures with $\{10\bar{1}0\}$ and $\{11\bar{2}0\}$ side facets. Our complex growth technology uses the gaseous HCl and NH_3 species, which are produced after the pyrolytic decomposition of NH_4Cl. However, the exact species that restrict the growth of ZnO along the *c*-axis and promote the lateral growth of ZnO in our experiments are still under investigation. As in the case of ZnO nanobelts, these hexagonal disks were also scraped off the substrate and prepared for the photo- decolorization experiments.

The ZnO tetrapods were the third nanomaterial, which were examined for photocatalytic activity. Generally, tetrapods are classified into three main groups: the first with uniform arm diameter, the second with tapered conical arm (nano-spike or nano-needle-like), and the last tetrapods, which one or several times abruptly change the arm morphology (lengths, thickness, shape) during growth. SEM images of tetrapods synthesized by our plasma-assisted technology are shown in Fig. 3a,b. They possess a sharp needle shape arm and accordingly could be attributed to the second type of tetrapods, which is known to have a very high photodecolorization activity [24, 25].
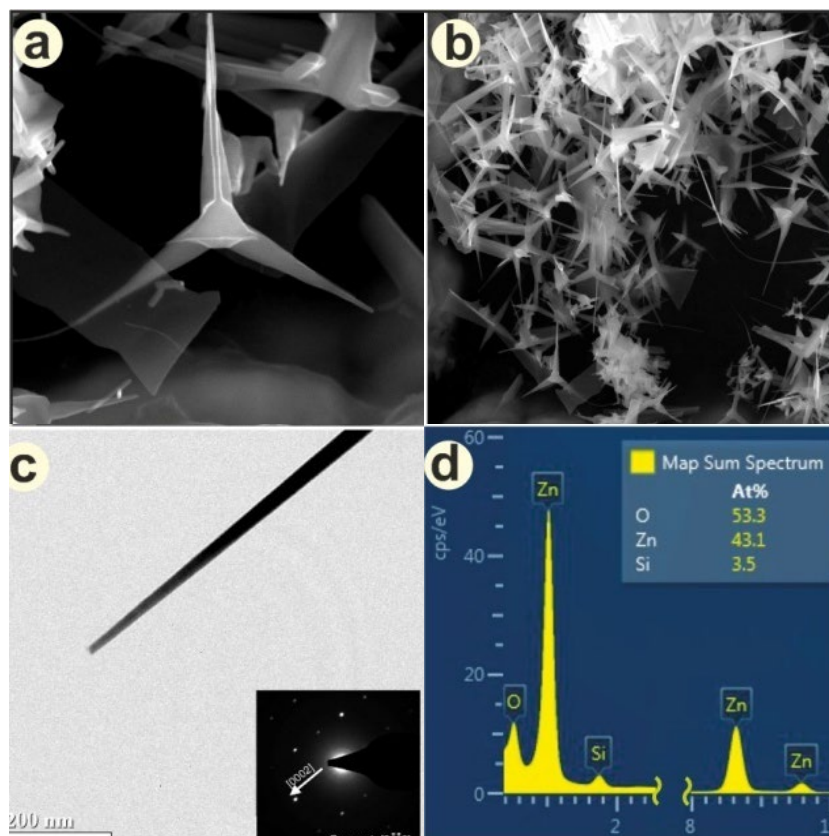
Fig. 3. (a,b) SEM images of tetrapods; (c) TEM image of a tetrapod arm and its SAED pattern (inset); (d) EDS spectrum of tetrapods. The Si peak originates from the silicon substrate.

The average size of tetrapods varies in the range of 4-5 micrometers. Some of the arms are ended with several micrometer-long ZnO nanowires. TEM image of a tetrapod tip and its SAED pattern are shown in Fig. 3c. As can be seen, the arm grows in the [0001] direction. The EDS spectrum of tetrapods, presented in Fig. 3d shows the increased value of oxygen, which is caused by the high porosity of tetrapodal network and hence, by the increased oxygen adsorption from the atmosphere. The peak of Si originates from the silicon substrate.

The photocatalytic activity of tetrapod structures is caused by better electron extraction, improved charge transport, ability to produce a highly connected network with an increased porosity and surface area [26]. The needle or pyramidal shape of arms can be considered an additional advantage of tetrapods. It is known, that the semi-polar pyramidal planes of ZnO, e.g.$\{10\bar{1}1\}$ and $\{11\bar{2}2\}$ have a high photocatalytic activity [27]. The pyramidal plane consists of altering $\{01\bar{1}0\}$ and $\{10\bar{1}1\}$facets [28]. The existence of semi-polar $\{01\bar{1}1\}$ crystal facets, which have high surface energy, can further increase the photocatalytic activity of tetrapods.

The results of our experiments on the photodegradation of methylene blue using ZnO with different morphologies are presented in Fig. 4. As we outlined previously, the illumination was performed using the Xe lamp, which has an emission spectrum close to the natural sunlight. The absorbance A_t was measured after each 20 min interval. The cumulative exposure time was 120 min.
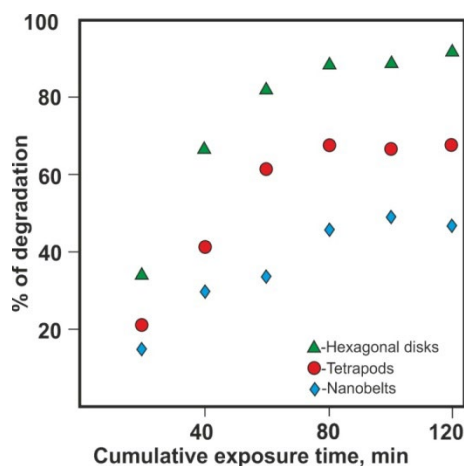
Fig. 4.The dependence of the photodegradation rate of ZnO nanomaterials with different morphologies on the cumulative light exposure time.

According to Fig. 4, the hexagonal ZnO disks have the highest photocatalytic activity, followed by the activities of tetrapods and nanobelts. This is consistent with the chemical activities of different crystal facets. The closely packed hexagonal disks (Fig. 2a) have the lowest specific surface area among other nanostructures. However, the high chemical activity of basal (0001) planes of hexagonal disks prevails over the low surface area and yields the highest catalytic activity. Comparing the activities of ZnO tetrapods and nanobelts, it should be noted that both of them were growing in the same, most abundant [0001] direction. However, as previously mentioned, the exposed semi-polar $\{01\bar{1}1\}$ facets of tetrapods, together with better electron extraction and improved charge transport [26], result in a higher catalytic activity of tetrapods as compared to nanobelts. For all samples, the photocatalytic activity increases with time and then reaches a saturation value after approximately 80 minutes of exposure. The observed saturation in catalytic decomposition may be related to the breakdown of ZnO in the water-based solution [29].

4. Conclusions

Pyrolytic technology was used for producing ZnO nanobelts and hexagonal disks. The process was performed in an active ambient formed after the thermal decomposition of NH_4Cl. The Si substrate temperature was 420°C and the mass ratio of Zn to ZnO in the source was 1.6 for nanobeltsand 0.5 for hexagonal disks. The nanobelts were growing along the c-axis through the Vapor-Liquid-Solid mechanism and they had Zn catalyst tips. Their sidewalls comprise $(2\bar{1}\bar{1}0)$ and $(01\bar{1}0)$ facets, while the average thickness was 35 nm. ZnO hexagonal disks had a mean diameter and thickness of 1.5 micrometers and 200 nm, respectively. Their flat surfaces were formed by (0001) facets, indicating that in our technology the growth along the thermodynamically preferable [0001] direction was suppressed. The tetrapods, with sizes in the range of 4-5 micrometers, were produced by plasma-assisted technology. They had tapered arms, which were growing along [0001] direction.

The decolorization of methylene blue solution under a solar light simulator confirmed a high photocatalytic activity of ZnO hexagonal disks, caused by the increased exposure of energetic (0001) facets. The activity of tetrapods was lower than that of ZnO disks, however, it was slightly higher than the photocatalytic activity of nanobelts. This can be explained not only by the well-known fact that tetrapods have better electron extraction and improved charge transport but also by the partially exposed semi-polar $(10\bar{1}1)$ facets of tapered arms. Their activity prevails over the photocatalytic activity of nanobelts, which contain only non-polar side facets.

References

[1] M.T. Noman, N. Amor, M. Petru. Critical Reviews in Solid State and Materials Sciences **47**, 99 (2021);   https://doi.org/10.1080/10408436.2021.1886041

[2] K. M. Mohamed, J. J. Benitto, J. J. Vijaya, M. Bououdina. Crystals **13**(2)**,** 329 (2023); https://doi.org/10.3390/cryst13020329

[3] A. Galdamez-Martinez, G. Santana, F.Güell, P.R. Martinez-Alanis, A.Dutt. Nanomaterials **10**(5), 857 (2020);   https://doi.org/10.3390/nano10050857

[4] V. Parihar, M. Raja, R. Paulose. Reviews on Advanced Materials Science **53**(2), 119 (2018); https://doi.org/10.1515/rams-2018-0009

[5] M. Terracciano, S. Rackauskas, A.P. Falanga, S. Martino, G. Chianese, F. Greco, G. Piccialli, G. Viscardi, L. De Stefano, G. Oliviero, N. Borbone, I.Rea. International Journal of Molecular Sciences **24**(5), 4449 (2023);   https://doi.org/10.3390/ijms24054449

[6] A. Buter, G. Maschkowitz, M. Baum, Y. K. Mishra, L. Siebert, R. Adelung, H. Fickenscher. International Journal of Molecular Sciences **24**(4), 3444 (2023); https://doi.org/10.3390/ijms24043444

[7] G. Dutta, A. Sugumaran. Journal of Drug Delivery Science and Technology **66**, 102853 (2021);   https://doi.org/10.1016/j.jddst.2021.102853

[8] Z. Hafizi, N. Nasr. Engineering, Technology & Applied Science Research **8**(1), 2508 (2018); https://doi.org/10.48084/etasr.1571

[9] N. Babayevska, L. Przysiecka, I. Iatsunskyi, G. Nowaczyk, M. Jarek, E. Janiszewska, S. Jurga. Scientific Reports **12**, 8148 (2022);   https://doi.org/10.1038/s41598-022-12134-3

[10] S. Goel, B. Kumar. Journal of Alloys and Compaunds**816**, 152491 (2020); https://doi.org/10.1016/j.jallcom.2019.152491

[11] R. Ridolfo, S. Tavakoli, V. Junnuthula, D. S. Williams, A. Urtti, J.C. M. van Hest. Biomacromolecules**21**(1),126 (2020);   https://doi.org/10.1021/acs.biomac.0c00726

[12] A. Sulciute, K. Nishimura, E. Gilshtein, F. Cesano, G. Viscardi, A. G. Nasibulin, Y. Ohno, S. Rackauskas. Journal of Physical Chemistry C **125**(2), 1472 (2021); https://doi.org/10.1021/acs.jpcc.0c08459

[13] R. Revathy, M. R.Varma, K. P. Surendran. Materials Research Bulletin **120**, 110576 (2019); https://doi.org/10.1016/j.materresbull.2019.110576

[14] S-H. Na, S-H. Park. Journal of the Korean Physical Society **54**(2), 867 (2009); https://doi.org/10.3938/jkps.54.867

[15] J. S. Loquero. Engineering, Technology & Applied Science Research **12**(4), 8990 (2022); https://doi.org/10.48084/etasr.5063

[16] M. M. Nadareishvili, G. Mamniashvili, D. Jishiashvili, G. Abramishvili, C. Ramana, and J. Ramsden. Engineering, Technology & Applied Science Research **10**(2), 5524 (2020); https://doi.org/10.48084/etasr.3392

[17] A.Jishiashvili, A. Chirakadze, Z. Shiolashvili, N. Makhatadze, V. Gobronidze, D. Jishiashvili. Proceedings of the 7th International Conference MTP-2021: Modern Trends in Physics. 125 (2021).

[18] G. Gelashvili, D. Gelenidze, S. Nanobashvili, I. Nanobashvili, G. Tavkhelidze, Ts. Sitchinava. International Journal of Chemical and Molecular Engineering **12**, 278 (2018); https://doi.org/10.5281/zenodo.1316875

[19] T. Khudkham, D. Channei, B. Pinchaipat, R. Chotima. ACS Omega **7**(37), 33258 (2022); https://doi.org/10.1021/acsomega.2c03770.

[20] S. Sucharitakul, R. Panyathip, S. Choopun. Materials **11**, 1360 (2018); https://doi.org/10.3390/ma11081360

[21] A. Wander, F. Schedin, P. Steadman, A. Norris, R. McGrath, T. S. Turner, G. Thornton, N. M. Harrison. Physical Review Letters **86**(17), 3811 (2001); https://doi.org/10.1103/PhysRevLett.86.3811

[22] S. G. Leonardi. Chemosensors**5**(2), 17 (2017); https://doi.org/10.3390/chemosensors5020017

[23] S. Luo, R. Chen, L.Xiang, J. Wang. Crystals **9**(11), 552 (2019); https://doi.org/10.3390/cryst9110552

[24] Y. K. Mishra, G. Modi, V.Cretu, V. Postica, O.Lupan, T. Reimer, I. Paulowicz, V. Hrkac, W. Benecke, L. Kienle, R. Adelung. ACS Applied Materials & Interfaces **7**(26), 14303 (2015); https://doi.org/10.1021/acsami.5b02816

[25] S-G. Heo, S-I. Jo, G-H. Jeong. Current Applied Physics **46**, 46 (2023); https://doi.org/10.1016/j.cap.2022.12.004

[26] K. Lee, M. Sahu , S. Hajra, R. Abolhassani, K. Mistewicz, B. Toron, H-G. Rubahn, Y. K. Mishr, H. J. Kim. Journal of Materials Research and Technology **22**, 811 (2023); https://doi.org/10.1016/j.jmrt.2022.11.142

[27] T. Lim, P.S. Mirabedini, K. Jung, P. A. Greaney, A.A. Martinez-Morales. Applied Surface Science **536**, 147326 (2021); https://doi.org/10.1016/j.apsusc.2020.147326

[28] E. Debroye, J. Van Loon, H.Yuan, K. P. F. Janssen, Z. Lou, S. Kim, T, Majima, M.B.J. Roeffaers. Journal of Physical Chemistry Letters **8**(2), 340 (2017); https://doi.org/10.1021/acs.jpclett.6b02577

[29] K.M. Lee, C.W. Lai, K.S. Ngai, J.C. Juan. Water Research **88**, 428 (2016); https://doi.org/10.1016/j.watres.2015.09.045